Showcasing research from Dr. Celso Ricardo Caldeira Rêgo, Institute of Nanotechnology and Platform MaterialDigital, Karlsruhe Institute of Technology, Germany.

Digital workflow optimization of van der Waals methods for improved halide perovskite solar materials

Hybrid organic–inorganic perovskites promise high efficiency at low cost but demand deeper insights into organic cation–inorganic interactions. Using a robust workflow powered by SimStack, we examine XH_4PbI_3 and $CH_3XH_3PbI_3$ (X = N, P, As, Sb) with DFT+vdW+SOC and DFT-1/2, uncovering critical impact of ionic radius and electronegativity on thermodynamic stability. This reveals how organic cation properties shift perovskite stability from NH_4PbI_3 toward Sb-based materials, opening pathways beyond $CH_3NH_3PbI_3$. This underscores workflow-driven efficiency in exploring next-generation perovskites.

Image reproduced by permission of Celso Ricardo caldeira Rêgo from *Digital Discovery*, 2025, **4**, 927.

ROYAL SOCIETY OF CHEMISTRY

rsc.li/digitaldiscovery

Digital workflow optimization of van der Waals methods for improved halide perovskite solar materials†

Celso R. C. Rêgo, [ID] *[a] Wolfgang Wenzel, [ID] [a] Maurício J. Piotrowski, [ID] [b] Alexandre C. Dias, [ID] [c] Carlos Maciel de Oliveira Bastos, [ID] [c] Luis O. de Araujo[d] and Diego Guedes-Sobrinho [ID] [d]

Hybrid organic–inorganic metal halide perovskites are low-cost and highly efficient materials used in solar cell devices. However, the intricacies of perovskites that merge organic cations with inorganic frameworks necessitate further elucidation, particularly from the long-range van der Waals perspective. Here, we scrutinize the van der Waals (vdW) methods by conceptualizing organic cations for XH_4PbI_3 and $CH_3XH_3PbI_3$ prototype perovskites (X = N, P, As, and Sb), to investigate the thermodynamic stability. To handle the enormous amount of raw data generated from DFT + vdW + SOC with DFT-1/2 (quasi-particle correction method), we have used the SimStack workflow framework, which enhanced the efficiency, reproducibility, and data transferability. The results reveal the critical role of the organic cations, inferred from ionic radius estimates and documented electronegativity, in elucidating the accommodation of symmetric XH_4^+ or asymmetric $CH_3XH_3^+$ cations within the limited volumes of cuboctahedral cavities. The discrepancy in the ionic size within the XH_4PbI_3 ($CH_3XH_3PbI_3$) group positions NH_4PbI_3 ($CH_3NH_3PbI_3$) outside (within) the stable perovskite region suggests the theoretical viability of perovskites containing phosphonium, arsonium, and stibonium beyond $CH_3NH_3PbI_3$. As we move from N to Sb, the organic cation's properties, such as ionic radius and electronegativity, affect the thermodynamic stability and local geometry of octahedra, directly influencing the band gaps.

1 Introduction

Metal halide perovskites (MHPs) have received unparalleled attention today, especially by the emergence of hybrid (organic–inorganic) MHPs,[1,2] since they constitute the most promising candidates for application in the third generation of photovoltaic solar cells, where their power conversion efficiency evolved from 3.8%[1] up to amounts exceeding 21% in less than a decade-and-a-half of study,[3–5] for instance, in the case of $FAPbI_3$, it surpassed 26% when applied in single-junction devices.[6] Concomitantly, the interest in hybrid MHPs for use as a solar cell absorber has been boosted rapidly because of their unique physical and chemical properties, the wide possibility of compositional modification, and production feasibility through simple benchtop chemistry.[7–9] However, the complexity arising from the addition of organic cations within an inorganic template leads to a high degree of difficulty faced by theoreticians and experimentalists, even more so in the attempt to correlate the acquired understanding at electronic and atomistic levels with empirical verified physico-chemical properties,[10,11] such as in contexts of tunable band gaps[12] and long carrier lifetimes.[13,14]

Among the possible organic–inorganic MHPs, methylammonium lead triiodide ($CH_3NH_3PbI_3$) has been the flagship of research, with a lower proportion of acclaim directed to other molecular cations (*e.g.*, formamidinium or acetamidinium).[7–9] In general, the attention is focused on the compositional engineering of the divalent-metal cation (Pb^{2+}) substitution by alternative species (*e.g.*, Ge^{2+} and Sn^{2+}),[15,16] or by the exchange of the halide anion (*e.g.*, I^- by Cl^- or Br^-),[1,17] or even by compositional alloys.[18–20] However, few studies have focused on the automatic design of the MHP composition in the sense of improving solar cell efficiencies and tuning absorption energy.[21,22] Given the flexibility of the organic cation choice, it is possible to consider a variety of organic molecules with different sizes, symmetries, and chemical features, which can directly influence the octahedral framework from distortions

[a]Karlsruhe Institute of Technology (KIT), Institute of Nanotechnology (INT), Hermann-von-Helmholtz-Platz 1, 76344 Eggenstein-Leopoldshafen, Germany. E-mail: celso.rego@kit.edu

[b]Department of Physics, Federal University of Pelotas, PO Box 354, Pelotas, RS, 96010-900, Brazil

[c]Institute of Physics and International Center of Physics, University of Brasília, Brasília 70919-970 Distrito Federal, Brazil

[d]Chemistry Department, Federal University of Paraná, Curitiba, PR, 81531-980, Brazil

and reorientations until charge balance, energy stabilization, and dimensionality changes in MHPs, leading to profound effects on the electronic structure.[8,9] Consequently, in principle, one could model the strength of organic–inorganic interactions by designing organic cations. This fact would imply the possibility of moving between structures with a minimal octahedral tilt, implying low-gap perovskites (optimum photovoltaic efficiency), or structures with a maximum tilt, implying large-gap perovskites (application in visible spectrum light-emitting diodes).[21]

In addition to the direct motivation of molecular cation design/substitution to tune optoelectronic properties,[21–24] there is a genuine motivation that resides in altering the cations, varying their constitutional chemical nature to increase the stability of the system as a whole without compromising the desirable range of band gaps for solar cell applications.[25] Even excluding any significant contribution of organic cations to the electronic structure (specifically around the band edges) and confirming their role in structural electrostatic stabilization,[26,27] we should consider the indirect role that organic cations (and their tuning) can play in electronic properties by inducing structural changes in inorganic octahedra through electronic coupling, hydrogen-bonding, and van der Waals (vdW) interactions.[25,28,29] For instance, it is shown that in the theoretical treatment of hybrid MHPs, based on density functional theory (DFT), the vdW correction inclusion changes the $CH_3NH_3^+$ spatial orientation, distorting the PbI_6 octahedra, leading to a direct–indirect band gap transition.[28] Thus, similar to the experimental situation in which hybrid MHPs are sensitive to processing conditions, computational modeling approaches to treat hybrid MHPs are also sensitive to the theoretical level. Hence, for hybrid MHPs, only a thorough study considering vdW corrections can achieve good agreement with experimental data, as reported by the first study combining dispersive interactions and spin–orbit coupling (SOC) treatments.[30]

Despite the well-established DFT success as an investigative/predictive tool,[31–34] being considered a workhorse in computational materials science, its proper application through standard (plain) DFT calculations based only on local, semilocal, and hybrid exchange–correlation functionals needs care,[31] since it misdescribes (or does not describe) long-range electronic correlation effects, for example, which means not counting the London dispersion interactions.[35–38] In the last few decades, there have been enormous efforts to improve the description of the vdW interactions through nonlocal vdW-DF functionals[39–41] and *a posteriori* approaches within the DFT framework, which have resulted in a variety of *a posteriori* methods, which we will focus from now on.[35,36,42–45] These corrections are based on the atom-pairwise potential interactions, where the vdW dispersion energy correction, E_{disp}, is added to the DFT total energy: $E_{tot} = E_{DFT} + E_{disp}$,[46–48] and they can be divided in (i) empirical approaches, having as main representatives D2, D3, and D3BJ frameworks proposed by Grimme,[42,43,49] where D2 (ref. 42) does not take into account environmental effects, which were subsequently introduced in the D3 (ref. 43) and D3BJ[49] frameworks through the addition of the coordination number dependence from the dispersion energy contributions in nth-order terms. The use of higher nth-order terms has presented an overestimation of lattice parameters for weakly bound bulk systems, so D3 has been recommended.[43,50] At the same time, for D3BJ, replacing the damping function with the Becke–Johnson (BJ) model provided better results for molecular systems involving non-bonded distances.[49]

On the other hand, we have (ii) the semi-empirical approaches, with (ii.1) TS, TSSCS, and MBD proposals by Tkatchenko and Scheffler,[35,36,51] where the vdW correction is determined from the ground-state electron density of the system, which allows capturing hybridization effects, as well as the environmental effects, by accounting for polarizability through the Hirshfeld volume.[35,36,52] TS does not include interactions beyond the local environment, disregarding the fluctuating dipole interaction effects. In contrast, TSSCS includes the self-consistent screening (SCS) effects, where the dipole long-range fluctuations are considered to have polarizability.[36] The many-body dispersion (MBD)[51] method is based on the random phase expression of the correlation energy and the dynamic response is approximated by that of dipole-coupled quantum harmonic oscillators, representing a more general approach that goes beyond the pairwise-additive treatment of dispersion. To complement (ii.2) the dDsC proposed by Steinmann and Corminboeuf[44,45] with similarities to the D2 method, except by the dispersion coefficients and damping function, which are charge-density-dependent. Therefore, to obtain the adequate refinement level, in addition to theoretical treatments that advance the DFT, one must consider the role played by vdW corrections.

Thus, herein, considering the standard DFT calculations and the main empirical (D2, D3, and D3BJ) and semi-empirical (TS, TSSCS, MBD, and dDsC) vdW corrections, within extra-relativistic corrections (SOC and quasiparticle DFT-1/2 (ref. 53)), we have accomplished a systematic investigation to assess the properties of the two archetypal hybrid MHPs. The chosen structural sets are based on a polar methylammonium cation $(CH_3NH_3^+)$[54] and its smaller nonpolar analog ammonium cation (NH_4^+),[23,26,55] combined with the lead iodide (PbI_3^-) inorganic part. For this, there is an experimental relationship between transformation[56] and reverse transformation[57] of NH_4PbI_3 to $CH_3NH_3PbI_3$ perovskites. For this purpose, we considered the family generated from ammonium – NH_4^+ (methylammonium – $CH_3NH_3^+$) by descending the pnictogen column in the periodic table, *i.e.*, including the hypothetical compounds formed by phosphonium – PH_4^+ (methylphosphonium – $CH_3PH_3^+$), arsonium – AsH_4^+ (methylarsonium – $CH_3AsH_3^+$), and stibonium – SbH_4^+ (methylstibonium – $CH_3SbH_3^+$), constituting the XH_4PbI_3 and $CH_3XH_3PbI_3$ (X = N, P, As, and Sb) set of MHPs. Consequently, we intend to obtain a complete overview of the effects of different vdW flavors in characterizing archetypal MHP structures, considering the complete picture that permeates among thermodynamic stability, structural feasibility, and maintenance of the band gap within a viable range for application in solar cells.

In our detailed investigation of metal halide perovskites (MHPs), we focused on the complex interactions between organic and inorganic components within hybrid systems. We

examined the dynamic interplay involving non-symmetrical, polar, and symmetrical, and non-polar organic molecular families central to the perovskite structure. This study revealed opportunities for manipulating orientational disorder and polarization through the custom design of organic cations by altering their chemical properties, directly impacting the structural motifs of the inorganic components and indirectly influencing the electronic structure. However, selecting the most compelling theoretical approach to address dispersive interactions within this organic–inorganic nexus remains a significant challenge due to the structural complexity of hybrid perovskites.

We integrated all simulation protocols into the SimStack modules called Workflow Active Nodes (WaNos) to manage this complexity.[58] Implementing scientific workflows contributes to making their data FAIR (Findable, Accessible, Interoperable, and Reusable) by automating and standardizing the execution of complex computational protocols. Workflow frameworks, such as SimStack,[58] AiiDA,[59] Pyiron,[60] and others, ensure that the entire simulation process is well-documented, reproducible,[61–63] and enriched with metadata. These workflows capture data provenance, detailing the parameters, software, and computational environments used at every step, which is critical for ensuring traceability and reproducibility. Furthermore, by integrating high-throughput and multiscale modeling, workflows streamline the generation and management of large datasets, which can then be stored in repositories such as GitHub, Materials Cloud, or NOMAD. This approach promotes data reuse and reduces non-expert users' barriers to leveraging advanced computational methods, ensuring broader accessibility and improved scientific collaboration. The user-friendly interface and versatile capabilities of SimStack facilitated the execution of complex computational workflows, aligning our research with the FAIR (Findable, Accessible, Interoperable, and Reusable) and TRUE (Transparent, Reproducible, Usable by others, and Extensible) principles,[61,64–69] thereby enhancing the scientific rigor of our study. Using Sim-Stack, we systematically explored the effects of different van der Waals corrections on the properties of typical hybrid MHPs with unprecedented precision and efficiency, paving the way for further theoretical investigations into this intriguing class of materials.

2 Theoretical approach, computational details, and workflow

Fig. 1 illustrates the workflow built within the SimStack[58] framework, designed to streamline the virtual screening process for van der Waals (vdW) methods within the exploration of various metal halide perovskite (MHP) cation compositions. This strategic approach facilitates a systematic investigation of stability, structural, and electronic characterization, thereby enabling the rapid prototyping of many vdW corrections. Such simulations are interconnected through multimodule workflows, significantly enhancing the efficiency of raw data production. The first segment, Fig. 1, part (1), engages in geometry optimization using a chosen vdW approach. It begins by selecting an A-site cation, which can be either CH_3XH_3 or XH_4, where X symbolizes elements such as N, P, As, or Sb. The process continues through Mult-It WaNo, which iteratively processes the molecular geometry with UnpackMol. Following this, DFT-VASP performs the geometry optimization, with the DB-Generator compiling the outcomes into a structured dataset.

The second segment, Fig. 1, part (2), of the workflow, illustrated on the right side of Fig. 1, utilizes the optimized structure from the first part. Herein, Mult-It embarks on iterative calculations to determine the band gap employing the DFT-1/2 method, complemented by a single-shot calculation via DFT-VASP. The results are then channeled into the DB-Generator. The automated flow of information is critical; the two .yml dataset files produced by the DB-Generator WaNo are pushed to a GitHub repository. From there, a Colab notebook can readily fetch the data for further analysis, such as estimating the bandgap energy and plotting the corresponding figure, as showcased for the MAPbI$_3$ case.

The project's documentation is available to the public via the GitHub repository at **https://github.com/KIT-Workflows/Halide-Perovskites**. This repository provides all the Workflow Active Nodes (WaNos) used in this project. In addition, the SimStack framework – a free and open-source workflow engine – is documented with a detailed guide and tutorials are hosted at **https://simstack.readthedocs.io**. This documentation offers a straightforward step-by-step walkthrough, encapsulates best practices, and provides comprehensive operational details, ensuring that the framework's full potential can be harnessed for advanced materials science research and development.

2.1 Total energy calculations

We carried out DFT-based[70,71] total energy calculations and structural optimizations within the semilocal exchange–correlation (xc) functional from the generalized gradient approximation[72] formulated by Perdew, Burke, and Ernzerhof[73] (PBE) as implemented in the Vienna Ab initio Simulation Package (VASP), version 5.4.1.[74,75] As previously highlighted, the semilocal xc functionals cannot provide a correct description of the nonlocal long range vdW interactions; consequently, several vdW energy corrections based on pairwise interactions have been proposed considering the dispersion energy (E_{disp}) in the energetic context of the plain DFT, $E_{tot} = E_{DFT} + E_{disp}$.[46–48] As a result, we have considered the most important (i) empirical approaches, i.e., D2 and D3 corrections proposed by Grimme[42,43] and the D3 correction including the Becke–Johnson (BJ) damping function (D3BJ), which is developed to improve the non-bonded distances.[49] In addition to the most relevant (ii) semi-empirical approaches, such as (ii.1) the Tkatchenko and Scheffler methods,[35,36,51] including Tkatchenko–Scheffler correction (TS), Tkatchenko–Scheffler with self-consistent screening (TSSCS), and many-body dispersion (MBD), where the term E_{disp} is based on ground state electron density of the system, and (ii.2) the Steinmann and Corminboeuf approach (dDsC),[44,45] which is very similar to the D2 method, except that
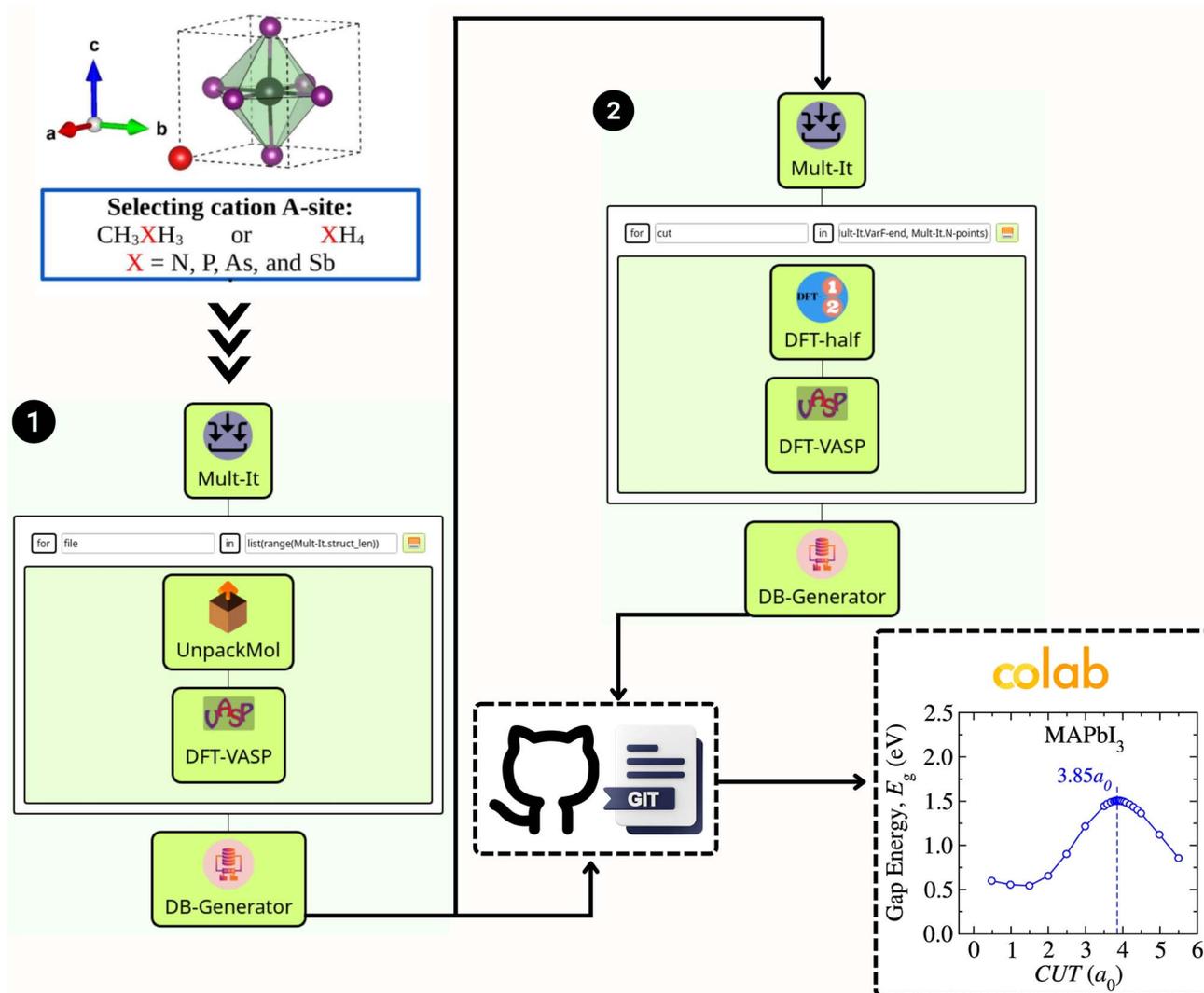
Fig. 1 SimStack workflow: the initial structures are used as input in part 1 (left side), which encompasses geometry optimization using a specified van der Waals (vdW) approach, starting with the selection of an A-site cation, either CH_3XH_3 or XH_4 (where X represents elements like N, P, As, or Sb), followed by file iterations in Mult-It WaNo for processing molecular geometry through UnpackMol, executing geometry optimization *via* DFT-VASP, and compiling results in a DB-Generator. The optimized structure from part (1) serves as input in part (2) (right side), which involves Mult-It for iterative calculations to determine the band gap using the DFT-1/2 method followed by one single shot calculation using DFT-VASP, with the outcomes also channeled into the DB-Generator. The two '.yml' dataset files generated *via* DB-Generator WaNo are automatically forwarded to the GitHub repo, from which a Colab notebook can access it for further analysis to estimate the gap energy and plot the gap energy, shown here for the $MAPbI_3$ case.

the dispersion coefficients and damping function are charge-density-dependent. Thus, we have performed a benchmarking considering D2, D3, D3BJ, TS, TSSCS, MBD, and dDsC vdW corrections, as implemented by Bučko *et al.* in VASP.[33,34,76,77]

To solve the Kohn–Sham (KS) equations, we employed the all-electron projector augmented wave method,[78,79] as implemented in VASP,[74,75,80] where the KS orbitals are expanded in plane waves up to a specific cutoff energy. By default, our plain DFT calculations are performed considering the scalar-relativistic approximation,[81,82] in which a fully relativistic calculation, including spin–orbit coupling (SOC), is taken into account for the core states. However, since SOC can play an essential role for Pb-based perovskites,[83–85] especially in non-

spherical atomic orbitals affecting the directionality of metallic bonds,[8] we have also included SOC for the valence states. We employed a plane-wave cutoff energy of 500 eV for the total energy calculations. At the same time, a stress tensor and atomic force optimization were performed to obtain the equilibrium bulk structures. A total energy convergence criterion of 1.0×10^{-5} eV was adopted in the KS self-consistent field cycle, while the equilibrium of Hellmann–Feynman forces was obtained once the atomic forces (on every atom) were smaller than 0.010 eV A^{-1}. For the Brillouin zone integration, a Monkhorst–Pack k-mesh of $4 \times 4 \times 4$ was employed, while a Gaussian smearing parameter of 50 meV was employed for all calculations. In addition to calculating the gap energies *via* plain DFT

and DFT + SOC, we also used the relativistic quasiparticle correction (DFT-1/2)[53] combined with SOC since it provides results with high precision, comparable to hybrid functionals such as HSE06 and the GW approach, requiring a low computational cost, which is similar to plain DFT. To verify the efficiency of this approach and obtain more details, please check our previous work.[16,86,87]

2.2 Atomic configurations

We have used a cubic structure based on the cubic unit cell ($1 \times 1 \times 1$) to model XH_4PbI_3 and $CH_3XH_3PbI_3$ (X = N, P, As, Sb), where the atomic configurations are presented in Fig. 2(a) and (b) as a result of two possible route paths for each case, respectively. The mechanisms for $XH_4PbI_3(s)$ formation

(Fig. 2(a)) can be based on $XH_3(g)$ and HI(g) precursors in the gas phase (named Route A),

$$XH_3(g) + HI(g) + PbI_2(s) \rightarrow XH_4PbI_3(s), \quad (1)$$
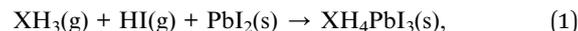
or based on the $XH_4I(s)$ precursor in the cubic solid phase (Route B),

$$XH_4I(s) + PbI_2(s) \rightarrow XH_4PbI_3(s). \quad (2)$$

Similarly, the mechanisms for $CH_3XH_3PbI_3(s)$ formation (Fig. 2(b)) can be based on $CH_3XH_2(g)$ and HI(g) precursors in the gas phase (Route A),

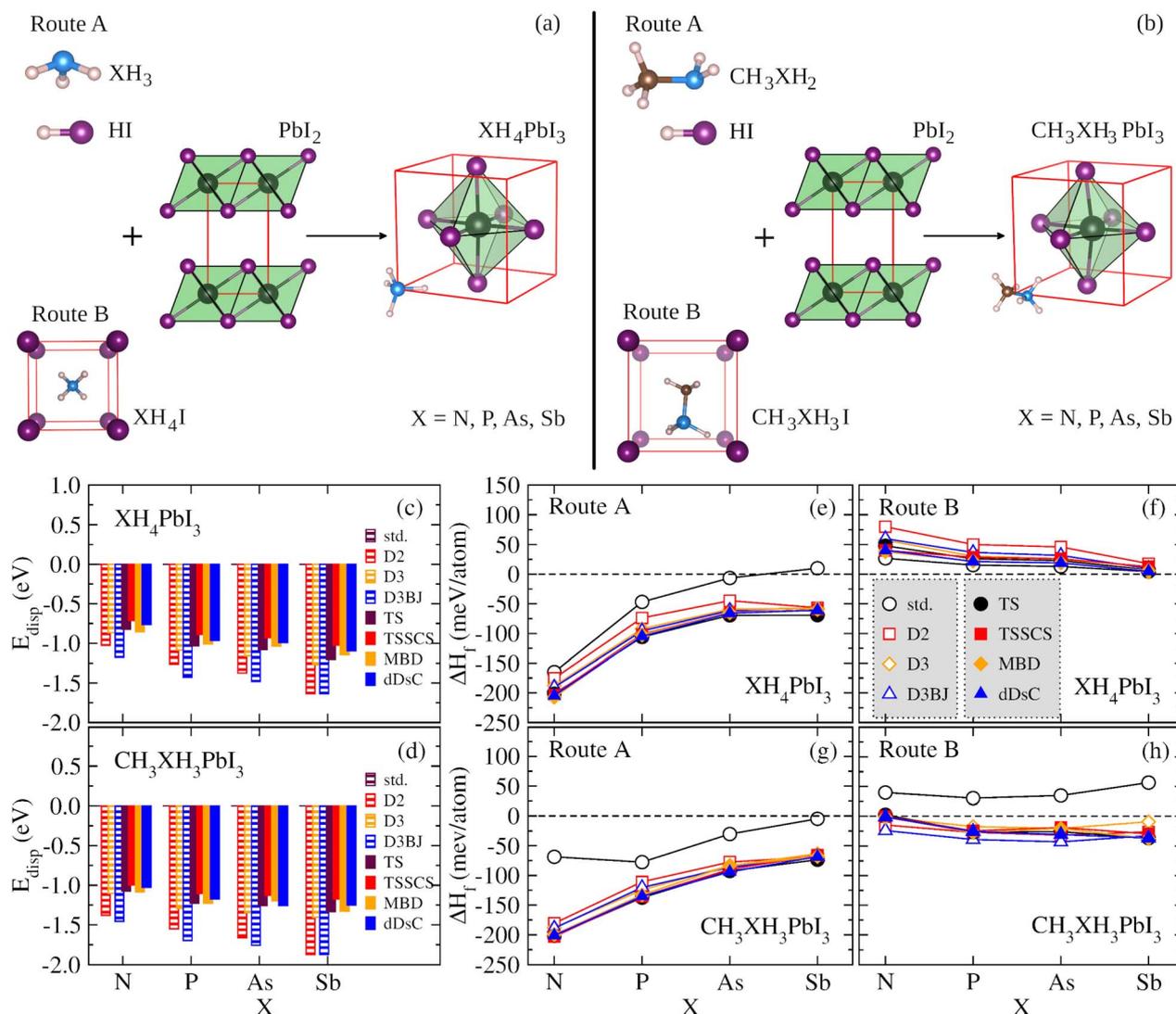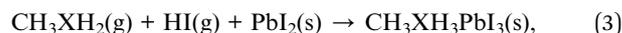$$CH_3XH_2(g) + HI(g) + PbI_2(s) \rightarrow CH_3XH_3PbI_3(s), \quad (3)$$

Fig. 2 The schematic representations of the mechanisms for (a) $XH_4PbI_3(s)$ formation, considering the $XH_3(g)$ and HI(g) precursors in the gas phase (Route A) and the $XH_4I(s)$ precursor in the cubic solid phase (Route B), and (b) $CH_3XH_3PbI_3(s)$ formation, considering the $CH_3XH_2(g)$ and HI(g) precursors in the gas phase (Route A) and the $CH_3XH_3I(s)$ precursor in the monoclinic or orthorhombic solid phase (Route B), where X = N, P, As, Sb. The dispersion energy contributions, E_{disp}, for the vdW correction flavours, D2, D3, D3BJ, TS, TSSCS, MBD, and dDsC are presented concerning X for (c) XH_4PbI_3 and (d) $CH_3XH_3PbI_3$ systems, where the plain DFT calculations are performed with the standard (std) PBE functional having $E_{disp} = 0$ eV. The formation enthalpies, ΔH_f, for XH_4PbI_3, obtained by (e) Route A and (f) Route B, and for $CH_3XH_3PbI_3$, obtained by (g) Route A and (h) Route B, are shown as a function of X, considering the std case and different vdW correction flavors.

or based on the $CH_3XH_3I(s)$ precursor in the monoclinic or orthorhombic solid phase (Route B),

$$CH_3XH_3I(s) + PbI_2(s) \rightarrow CH_3XH_3PbI_3(s). \quad (4)$$

The formation processes of the XH_4PbI_3 and $CH_3XH_3PbI_3$ atomic configurations were verified by calculating the formation enthalpies, ΔH_f (eV), considering the precursors involved in each route for both mechanisms through

$$\Delta H_f = E_{APbI_3} - \sum_i E_i, \quad (5)$$

where $A = XH_4$ or CH_3XH_3 (X = N, P, As, Sb) and E_i is the energy of the ith precursor in the formation process. The ΔH_f values were obtained from the total energy calculations taking into account the different flavors of vdW corrections (D2, D3, D3BJ, TS, TSSCS, MBD, and dDsC), where the vdW energetic contributions as well as the ΔH_f values for XH_4PbI_3 and $CH_3XH_3PbI_3$ are shown in Fig. 2(c)–(h) and discussed in the Results section.

Thus, our XH_4PbI_3 and $CH_3XH_3PbI_3$ archetypes are perovskite models with the inorganic lead iodide components forming a network of corner-sharing octahedra, where the diagonal and its perpendicular edges define, respectively, the apical and equatorial directions in the octahedron's frame, with the XH_4^+ and $CH_3XH_3^+$ cations located in the center of the inorganic cuboctahedral cavity. Concerning the orientation of the organic molecules in the inorganic cuboctahedral cavity, the initial setup of the molecular cations are free to rotate during the full geometry optimizations, $i.e.$, there are no constraints. For XH_4PbI_3, there is no significant orientation dependence of XH_4^+ due to its approximately spherical topology and nonpolar nature, as reported in the context of the ammonium ion.[55] For $CH_3XH_3PbI_3$, the orientational behavior of $CH_3XH_3^+$ is a little more intricate owing to its polar nature (molecular dipole) and non-spherical topology. However, as reported in ref. 28, the potential energy surface (energy landscape) is shallow for different possible orientations of organic cations. There is the possibility, for example, of (001)-, (111)-, or (011)-oriented molecules constituting flat local minima (almost equivalent), with energy differences of tens of meV.[23,28,55] As this energetic order represents values smaller than k_BT, we have that at 300 K the XH_4^+ and $CH_3XH_3^+$ are free to rotate, as evidenced experimentally for the methylammonium case.[88] Notwithstanding this, the organic–inorganic interactions have a relevant role in the results that will be presented, making it clear that the dispersive forces are critical for the internal geometry optimization of the studied systems.

3 Results

3.1 vdW energy contributions

To verify the contributions of various types of vdW energy corrections based on pairwise interactions, we calculated the E_{disp} term, from the $E_{tot} = E_{DFT} + E_{disp}$ context, taking into account the empirical (D2, D3, and D3BJ) and semi-empirical (TS, TSSCS, MBD, and dDsC) approaches, and the standard (std) DFT calculation (without vdW correction), for the XH_4PbI_3

and $CH_3XH_3PbI_3$ MHPs, considering different pnictogens, $i.e.$, X = N, P, As, and Sb, as shown in Fig. 2(c) and (d), respectively. We noticed that the vdW corrections contribute towards reducing the total energies to the calculation without vdW, $i.e.$, one improves the energy stabilization of the studied systems, given the improvement in the description of organic cations, inorganic framework, as well as their interactions (organic–inorganic). The E_{disp} accounting for the total energy ranges from 0 eV (std) to about 1.63 eV for XH_4PbI_3 and 1.87 eV for $CH_3XH_3Pb_3$ in the case of empirical corrections involving Grimme's family, which are larger (more pronounced) compared to semi-empirical corrections (maximum contributions of 1.20 eV for XH_4PbI_3 and 1.34 eV for $CH_3XH_3Pb_3$).

For both XH_4PbI_3 and $CH_3XH_3PbI_3$ sets, we observed the same trend of vdW flavors as a function of the X element, with some main characteristics, and the E_{disp} average magnitude range increases through different elements of the nitrogen family, $i.e.$, it increases from N to Sb, which is expected since the vdW corrections more pronouncedly assess the non-covalent inter- and intramolecular interactions. Furthermore, the magnitude of vdW corrections is larger for $CH_3XH_3PbI_3$ than for XH_4PbI_3, which is explained by the molecular nature of the organic cation itself, $i.e.$, $CH_3XH_3^+$ has a larger (lower) cation size (symmetry) than XH_4^+. Consequently, $CH_3XH_3^+$ undergoes further improvements to describe the electrostatic interactions (and beyond) between fluctuations in electronic charge density than XH_4^+, added to the higher interactions within the inorganic cuboctahedral cavity, which causes a larger distortion of the (inorganic) PbI_6 octahedra due to the accommodation of (organic) cations.

3.2 Formation enthalpies

Once the E_{disp} contributions have been identified, we need to explore the nature and influence of dispersion forces on the thermodynamic feasibility of the MHPs studied here. The formation enthalpy (ΔH_f) was considered from two possible formation routes (A and B) for XH_4PbI_3 and $CH_3XH_3PbI_3$, whose ΔH_f values are depicted in Fig. 2(e)–(h) as a function of group 15 elements. In general, the ΔH_f versus X trends in both routes are similar across the XH_4PbI_3 and $CH_3XH_3PbI_3$ sets for all vdW corrections, $i.e.$, on the one hand, we have the (almost completely exothermic) Route A that combines the molecular precursors in the gas phase with $PbI_2(s)$ and presents the compound with X = N as the most thermodynamically favorable, in accordance with what was observed experimentally for $CH_3NH_3PbI_3$,[89] with the ΔH_f magnitude decreasing with increasing atomic number X. On the other hand, we have the (endothermic, greatly for std) Route B, with precursors in the solid phase, with a reduced tendency for compound formation that is practically unalterable concerning the X exchange.

In addition to Route A being energetically favorable to Route B for all X elements and considering all vdW corrections, the thermodynamic stability trend for the XH_4PbI_3 exothermic (endothermic) process as a function of X is similar for calculations with and without vdW corrections, with additive (diminutive) contributions in the XH_4^+ description by different vdW

flavors that shift down (up) the negative (positive) ΔH_f values on Route A (Route B), with a significant emphasis on the SbH_4PbI_3 ΔH_f value, which is corrected from positive (std) to negative (all vdW flavors) in Route A. In the $CH_3XH_3PbI_3$ case, we also observed the higher thermodynamic stability of Route A compared to Route B, so that the vdW approaches correct for a more exothermic trend (downward shift in) the ΔH_f *versus* X behavior without vdW (std). This highlights the correction of the underestimated ΔH_f magnitude in Route A to $CH_3NH_3PbI_3$ and the complete change from endothermic (std) to exothermic (all vdW flavors) in the Route B formation mechanism.

Thus, considering the vdW corrections, the XH_4PbI_3 and $CH_3XH_3PbI_3$ compounds proved likely for the formation Route A considered here, where the ΔH_f magnitude obtained by semi-empirical vdW flavors is larger than those obtained by empirical vdW corrections, with both approaches describing the thermodynamic stability order: $NH_4PbI_3 < PH_4PbI_3 < AsH_4PbI_3 \lesssim SbH_4PbI_3$ and $CH_3NH_3PbI_3 < CH_3PH_3PbI_3 < CH_3AsH_3PbI_3 < CH_3SbH_3PbI_3$. Therefore, it is verified that the thermodynamic feasibility decreases with the change of X (from N up to Sb) in the organic cation composition within the MHP archetypes. To understand this stability variation with the molecular cation design used here (X variation) and how the different vdW type corrections can influence, we need to discuss (i) the nature of the organic cations, initially going through the feasibility of building XH_4PbI_3 and $CH_3XH_3PbI_3$ MHPs, through different ionic sizes and electronegativities (see Tables S1 and S2†); (ii) the structural analysis considering the lattice parameters and volume of the XH_4PbI_3 and $CH_3XH_3PbI_3$ bulks systems, with the changes arising in the inorganic counterpart (PbI_6 octahedra); (iii) the electronic behavior (through the energy gaps) for possible technological applications.

3.3 The nature of the organic cations

To complement the understanding of the stability trend obtained *via* molecular cation design and to expand the discussion about the contribution of different vdW corrections, it is necessary to infer the nature of the organic cations. Before that, it is essential to analyze the organic–inorganic configuration in cubic-motif perovskite, where all ions are treated as rigid spheres. For the inorganic framework, we have the halogen anion (I^-) occupying the vertices of regular PBI_6 octahedra, with the divalent metal cations (Pb^{2+}) in the center of the octahedra, where the volume enclosed by the neighboring octahedra defines the cuboctahedral cavity, which hosts the monovalent organic cation (XH_4^+ or $CH_3XH_3^+$). Thus, considering the ionic radii,[90,91] r_{ion} (see Table S1†), our MHP model structures are contained within the minimum radius ratio for the stability of the octahedron (geometric factor of octahedron formation, 0.414),[90] *i.e.*, the octahedral factor considered here, given by $\frac{r_{Pb,ion}}{r_{I,ion}}$, is equal to 0.54. Therefore, as evidenced by the relatively low octahedral distortion shown in Fig. S2,† the stability of the perovskite octahedra implies that the cuboctahedral cavities provide only a limited volume for the organic cations.[16,87] Consequently, accurately determining the size of these

molecular cations is essential to elucidate the interplay between the inorganic framework and the organic moieties in hybrid perovskites.

The ionic radius determination is a challenge, even for symmetrical cations (such as XH_4^+) and even more for non-spherically symmetric cations (such as $CH_3XH_3^+$), since we are dealing with molecular cations free to rotate about its center of mass, with bond lengths that can vary due to hydrogen-bonding interactions with the anionic counterparts. Therefore, to estimate the ionic radius of XH_4^+, r_{XH_4}, we have considered the X–H average bond lengths, $d_{av,X–H}$, in the context of $r_{XH_4} = \sqrt{2}d_{av,X–H}$; while for the $CH_3XH_3^+$ ionic radius, $r_{CH_3XH_3}$, we have considered two ways of estimating (i) based on the C–X bond lengths, $d_{C–X}$, and the r_{ion} of X elements, through $r_{CH_3XH_3} = 0.5d_{C–X} + r_{X,ion}$, and (ii) from the distance between the center of mass (CM) of the organic cation and the atom with the largest distance to CM (except for the H atoms), d_{CM}, being estimated from $r_{CH_3XH_3} = d_{CM} + r_{X,ion}$. Thus, the ionic radii for the organic cations have the $d_{av,X–H}$, $d_{C–X}$, and d_{CM} quantities calculated for X within empirical, semi-empirical, and without (std) vdW corrections (see Table S3†), presenting a variation of values smaller than 1.16% among the different approaches. As an inherited result, the r_{XH_4} and $r_{CH_3XH_3}$ values also showed a small variation (<0.69%) with different vdW corrections.

The ionic radius values follow the atomic size increase of pnictogens, *i.e.*, $r_{NH_4} < r_{PH_4} < r_{AsH_4} < r_{SbH_4}$ and $r_{CH_3NH_3} < r_{CH_3PH_3} < r_{CH_3AsH_3} < r_{CH_3SbH_3}$ (by (i)), in good agreement with the relative difference for ionic sizes concerning N, wherein P, As, and Sb are 45.21%, 52.05%, and 67.81%, respectively, larger than that of N.[90,91] Our r_{XH_4} and $r_{CH_3XH_3}$ results are in agreement with previous theoretical work[21] in the context of steric radii (within LDA), while our specific results for r_{NH_4} (146.79 pm) and $r_{CH_3NH_3}$ (220.43 pm by (i) and 224.53 pm by (ii)), using dDsC, are the closest to the effective radius values of 146 pm and 217 pm, respectively, taken as a reference.[9,92]

Once the ionic radii for the organic cations are estimated, we can verify the feasibility of perovskite formation through the archetypal models studied here, using the Goldschmidt tolerance criterion, ($t = (r_{XH_4/CH_3XH_3} + r)_I / \sqrt{2}(r_{Pb} + r_I)$), $0.8 \leq t \leq 1.0$,[8,9,93] which assesses whether the organic cation site can fit within the cavities of the inorganic structure. Consequently, from t, it is possible to evaluate the ionic size mismatches to indicate the different structural types, where a perfectly packed structure is obtained for $t \approx 1$, with mostly cubic structures for $0.9 < t < 1$ and distorted structures for $0.8 < t < 0.89$, whereas $t < 0.8$ (too small cation) and $t > 1$ (too large cation) refer to the formation of other structural motifs, *e.g.*, tetragonal and hexagonal, respectively.[7,8,92,94] It is important to note that obtaining a positive ascension for the formability criterion does not imply that the perovskite is the only stable phase for a given compound since perovskite has a propensity to undergo a series of phase transitions that can be modulated by chemical factors, temperature, and pressure.[8,9]

Our results for t as function of r_{XH_4} or $r_{CH_3XH_3}$ are depicted in Fig. 3 (numerical values in Table S3†) considering the different vdW corrections. The first finding is related to the small

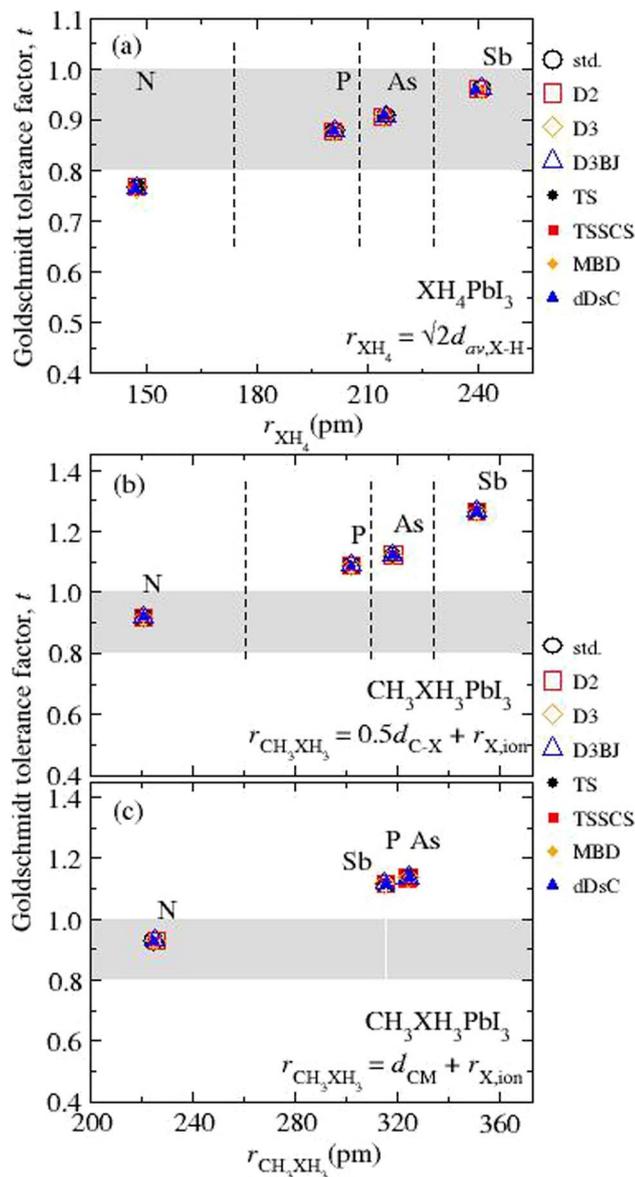**Fig. 3** Calculated Goldschmidt tolerance factors (t) concerning the ionic radius for the organic cations (r_{XH_4} and $r_{CH_3XH_3}$) for all the (a) XH_4PbI_3 and $CH_3XH_3PbI_3$ calculated from (b) $r_{CH_3XH_3} = 0.5d_{C-X} + r_{X,ion}$ and (c) $r_{CH_3XH_3} = 0.5d_{CM} + r_{X,ion}$, where X = N, P, As, and Sb. The mathematical expressions used to estimate the ionic radii of molecular cations are indicated inside each graphical part, while the ionic radii of the elements[90,91] can be found in Table S1.† The grey area corresponds to the geometric criterion for the Goldschmidt tolerance factor.[93]

perovskites. Thus, the cuboctahedral cavity has a size limitation concerning the organic cation size, *i.e.*, small organic cations are expected to fit better into the structure (except for NH_4PbI_3). In addition to $CH_3NH_3PbI_3$, some hypothetical perovskites with phosphonium, arsonium, and stibonium are predicted, in agreement with previous work.[21]

In general, it is observed that the interaction between the organic cations and the inorganic framework, which translates into the molecular cation confinement in the inorganic cavity, results in only slight structural changes of XH_4 and CH_3XH_3, even using different vdW flavors, as evidenced by the $d_{av,X-H}$, d_{C-X}, and d_{CM} results and their respective small variations concerning the std calculations (without vdW). Thus, the main influence inflicted on the organic part by coupling with the inorganic counterpart is related to the conformation of the organic component, with the bond formation between the I and H atoms. On the other hand, the inorganic framework undergoes larger structural changes due to the influence of organic cations, as we will discuss in the next subsection. Finally, through the t results, it is evident that the increases in the X ionic radius in group 15 elements for the $CH_3XH_3PbI_3$ set, previously associated with a decrease in thermodynamic stability (Route A), result in structural destabilization ($t > 1$ for X = P, As, and Sb). In the case of XH_4PbI_3 set, we also have the thermodynamic destabilization with the increase in the ionic size. However, t remains within the structural stability (cubic) limit ($0.9 \lesssim t < 1$), so, we need to add to the discussion the electronegativity of the X elements involved in the formation of the XH_4^+ cations.

Considering the Pauling electronegativity scale (see Table S2†) for the chemical elements of XH_4PbI_3 and $CH_3XH_3PbI_3$ sets, it is evident that altering the pnictogen changes the nature of the organic cations not only in terms of ionic radius but also in terms of electronegativity, as follows: N (3.04) > P (2.19) > As (2.18) > Sb (2.05).[95] Starting from the NH_4^+ cation, more commonly used in the XH_4PbI_3 compounds,[23,26,55] we have in its composition a strongly electronegative atom of N which compared to the electronegativity of I (2.66) will keep the H atoms tightly bonded in the organic cation, minimizing the interaction with the inorganic octahedron. Similarly, the $CH_3NH_3^+$ cation, most commonly employed in the $CH_3XH_3PbI_3$ set,[54] is composed of the strong electronegative atom of N and the moderate electronegative atom of C (2.55), so taking into account the I electronegativity, the H atoms will remain strongly bonded in $CH_3NH_3^+$, also resulting in a small organic–inorganic interaction. However, when the organic cations are modified, exchanging N for other less electronegative pnictogens, there will be a reduction in the X–H binding strength, which is evidenced, for example, by the increase in the $d_{av,X-H}$ values with the atomic number increasing from N to Sb (see Table S3†), causing an increase in interaction with the PbI_6 octahedron.

Thus, we verified the design of the organic cations by considering their ionic radius, and electronegativity provides the premises for understanding the thermodynamic stability trend of the XH_4PbI_3 and $CH_3XH_3PbI_3$ compounds *via* Route A. The ionic radius increases and the electronegativity decrease (from N up to Sb) in the organic cation composition leads to

variation in t values from different vdW flavors, ≤0.37%, corresponding to average t values of 0.766 for NH_4PbI_3, 0.878 for PH_4PbI_3, 0.907 for AsH_4PbI_3, 0.960 for SbH_4PbI_3, 0.919 (0.928) for $CH_3NH_3PbI_3$, 1.088 (1.135) for $CH_3PH_3PbI_3$, 1.123 (1.136) for $CH_3AsH_3PbI_3$, and 1.265 (1.116) for $CH_3SbH_3PbI_3$, where the values in parentheses are obtained through d_{CM}. The t values for NH_4PbI_3 and $CH_3NH_3PbI_3$ are in good agreement with the respective values ($t_{NH_4} = 0.763$ and $t_{CH_3NH_3} = 0.912$) obtained from the ionic radii reported in the literature.[91,92] Contrary to the other archetypes of the XH_4PbI_3 ($CH_3XH_3PbI_3$) group, NH_4PbI_3 ($CH_3NH_3PbI_3$) lies outside (inside) the stable region for

a decrease in thermodynamic stability, which are directly evidenced by the structural (cubic) destabilization for the CH_3-XH_3PbI_3 set (when $t > 1$ for $X \neq N$) and by the employment of less electronegative elements than N for the XH_4PbI_3 set (since the whole set still maintains the $t < 1$ condition). Both bring up the intensification of the ionic electrostatic interaction with the inorganic framework, resulting in the increase in its structural distortions and consequent stability decrease. To demonstrate and prove the trends that can be obtained from the electronegativity difference between two atoms, which can reflect from the polarity measure to the ionic character of the bond between them, we have calculated the charge population through the density-derived electrostatic and chemical (DDEC6)[96] method for the partial charge mapping of XH_4PbI_3 and $CH_3XH_3PbI_3$ MHPs, considering the atoms (of the organic cations) and ions individually, as can be found in Fig. S1.†

3.4 Structural analysis

To understand the structural changes of our perovskite models that arise from the design of organic cations, XH_4^+ and $CH_3XH_3^+$, as well as the influence of different vdW corrections, we have verified the a, b, and c lattice parameters along the (100), (010), and (001) directions, respectively, and the volume for all XH_4PbI_3 and $CH_3XH_3PbI_3$ MHPs as a function of X. The lattice parameters and volume results are shown in Fig. 4, where it is possible to verify the slight (average) increase in the structural volume that results from the modification of the organic cation by replacement of the smaller ionic radius pnictogen by a larger one in both sets, *i.e.*, increasing the atomic number in group 15 elements of the periodic table increases (on average) the volume. However, we observe that the volumetric increase due to X substitution (from N up to Sb) does not necessarily mean an increase of all lattice parameters (*e.g.*, see

(100): a for XH_4PbI_3) and also does not necessarily imply a similar increase along all directions (*e.g.*, compare (010): b and (001): c for $CH_3XH_3PbI_3$).

In terms of vdW corrections, it is noticeable that the lattice parameter values are decreased in relation to the std values, with few exceptions. The most significant decreases (maximum contractions) on average occur for empirical vdW corrections, with D2 presenting the most underestimated structural parameters, while semi-empirical corrections have an intermediate behavior (between the Grimme family corrections and calculations without vdW). The small leakages from a well-behaved trend of the lattice parameters and volume can be attributed to the different possible orientations of the organic cations within cuboctahedral cavities, which are a direct result of a full structural optimization – free of constraints. In addition, larger or smaller cations, in the context of $t \approx 1$, can lead to significant changes in the inorganic part (which we will discuss soon) because of the interaction strength variation between the organic and inorganic parts, governed by the electronegativity difference between interacting ions, which is reflected in the octahedral distortions.

From the structural parameters, we found that, regardless of whether or not there are vdW corrections, all the $CH_3XH_3PbI_3$ structures adopt a pseudo-cubic motif, where $a \neq b \neq c$; while all the XH_4PbI_3 structures adopt a tetragonal motif, where $a \neq b = c$. For both, the lattice constant values and volume (on average) correlate with the atomic sizes of the pnictogens, *i.e.*, $NH_4PbI_3(CH_3NH_3PbI_3) < PH_4PbI_3(CH_3PH_3PbI_3) < AsH_4PbI_3(CH_3AsH_3PbI_3) < SbH_4PbI_3(CH_3SbH_3PbI_3)$. Moving on to considering vdW corrections, the structural description is improved, correcting the calculated lattice constants, and the indirect impact of vdW interactions is mainly correlated with the unit cell volume, which is decreased (contracted) concerning the value obtained *via* std calculations.
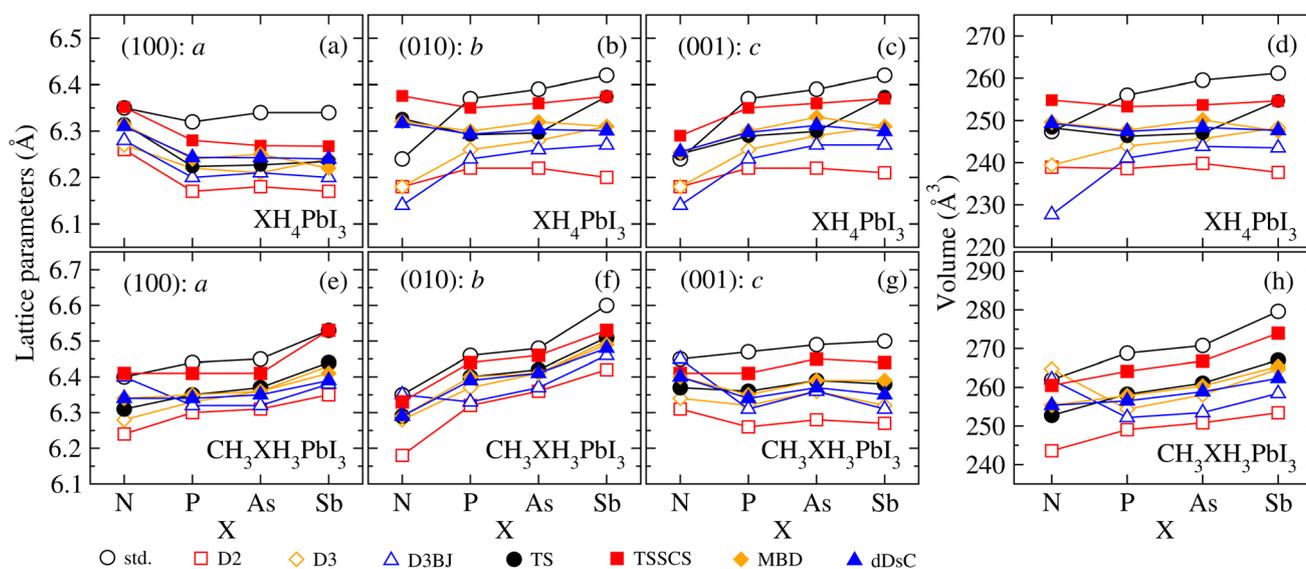

Fig. 4 Lattice parameters (a) (100): a, (b) (010): b, and (c) (001): c and (d) volume for all cubic XH_4PbI_3 MHPs, as well as the lattice parameters (e) (100): a, (f) (010): b, and (g) (001): c and (h) volume for all cubic $CH_3XH_3PbI_3$ MHPs, as a function of X (N, P, As, and Sb), calculated within empirical (D2, D3, and D3BJ) and semi-empirical (TS, TSSCS, MBD, and dDsC) and without (std) vdW corrections.

Our lattice constants for $CH_3NH_3PbI_3$ (where $c > a > b$) vary between 6.35 and 6.45 Å for std calculation, improving with the best vdW correction (D3) for values between 6.28 and 6.34 Å, which represent deviations between -0.63% and 0.32% in comparison with experimental report (6.32 Å).[97] The calculated lattice parameters for $CH_3NH_3PbI_3$ are also in good agreement with another experimental study based on powder and single crystal X-ray diffraction measurements: 6.26 Å (ref. 54) and 6.31 Å,[98] as well as the lattice parameters for $CH_3NH_3PbI_3$ and NH_4PbI_3 are found to be in good agreement with theoretical approaches.[26,55] It is important to note that DFT-based calculations are performed at 0 K, while experimental lattice constant values are measured at room temperature or above;[98] consequently, the reported experimental values may be influenced by thermal expansion.

Despite the initial orientational freedom for the organic cations within the cuboctahedral cavity, our results suggest that the relaxed structures are the result of the interactions (*i.e.*, the complementation) between the molecular cation and the inorganic framework, which are governed by the low symmetry of the organic cations, the inorganic framework deformations, and the symmetry reduction of the octahedra, all of them aiding the perovskite stabilization. Consequently, it is crucial to include vdW interaction in MHP simulations since they indirectly affect structural stability. When they comprise, the reduction of the unit cell volume influences the organic–inorganic interaction. As a result, it is necessary to verify two complementary structural aspects: the octahedral distortions from the strain that the organic cations exert on the inorganic part and the possible formation of hydrogen bonds between the organic and inorganic parts.

Specifically, to treat the structural distortions of the inorganic part, one can dose them by variations with the Platonic model[21,54] and its values of the Pb–I bond lengths and the Pb–I–Pb angles. Both properties are given regarding the plane formed by the *ac*-lattice parameter, named equatorial direction, and relative to the *b*-axis, named apical direction. From the X-ray diffraction data,[54] the Pb–I average bond length value is equal to 3.18 Å (or 3.16 Å[98]) with the largest relative deviations of 0.1%, which implies extremely regular bond distances. In addition, the Platonic model has collinear Pb–I–Pb bonds, which present a Pb–I–Pb angle of 180°. Consequently, the two diagonals of PbI_6 are practically perpendicular (maximum angular deviation of 4°).[54] However, contrary to the Platonic model, our results for equatorial and apical Pb–I bonds and Pb–I–Pb angles, as local structure parameters (see Tables S4 and S5†) show large deviations for XH_4PbI_3 and $CH_3XH_3PbI_3$, which reflect on the distortions suffered by the inorganic framework, given the interaction and accommodation of different organic cations.

The design of XH_4^+ and $CH_3XH_3^+$ cations by changing the nature of these organic cations through the ionic radius (electronegativity) increase (decrease) of X from N up to Sb reflects the (slight) increase of the lattice constants and volume. As a consequence, their octahedra are locally more distorted, as can be seen through the differences between the smallest and largest Pb–I distance values and Pb–I–Pb angles, both on equatorial and apical directions (Tables S4 and S5†). The angles

between the lattice constants, α, β, and γ, reveal negligible (appreciable) deviations in relation to the 90° – Platonic case – for our archetypes with $t < 1$ ($t > 1$).

Similar to the lattice parameter results, the different vdW corrections reduce the equatorial and apical Pb–I bond values compared to the calculation without vdW. These reductions reach maximum values of 4.1% (8.7%) for XH_4PbI_3 (CH_3XH_3-PbI_3) with the D2 correction. Thus, despite having the same inorganic framework for all archetypes here, we observed that all structures comprise distortions in Pb–I bonds concerning what would be expected from the Platonic case, with the closest proximity to the std values. The appearance of octahedral deformations is also reflected in the equatorial and apical Pb–I–Pb angles, with the largest leakages from the Platonic model appearing for systems with smaller organic cations (*e.g.*, NH_4PbI_3) and with the use of empirical vdW corrections or std calculations. On the other hand, we observed that the use of larger organic cations (*e.g.*, $CH_3AsH_3PbI_3$) leads to equatorial and apical angles closer to 180° since the bonds and bond angles of the inorganic part define the cuboctahedral cavity volume.

In general, the nature of organic cations, tuned by the ionic size and electronegativity of the X species, influences the inorganic framework reorientations. Added to the fact that the electronic properties are highly sensitive to the Pb–I modifications,[16,87] it is verified that in addition to the organic cation size, the effect of electronegativity differences between the ionic constituents is also relevant since they are associated with partial charges and polarizability. Consequently, one of the mechanisms that permeates the organic–inorganic interaction and that can reflect the connection between the nature of organic cations and distortion of the PbI_6 octahedra reside in the hydrogen bond formation. So, the strength of the hydrogen bonding is reported as an indication of the octahedral tilting.[99] Thus, considering the relevant bridging bond between the electron-donating element in the organic cation (X) and H atoms forming a bridge with the I, we present in Fig. 5 the average H–I bond lengths, $\langle d_{H-I} \rangle$, for XH_4PbI_3 and $CH_3XH_3PbI_3$ as a function of X for calculations without vdW and with empirical or semi-empirical vdW corrections.

Considering the XH_4^+ tetrahedral symmetry and their non-polar character, one would expect a centrally located geometric conformation in the inorganic cuboctahedral cavity with the four H atoms pointing in the interstitial regions. Although Fig. 5 confirms this situation by presenting an approximately similar general $\langle d_{H-I} \rangle$ magnitude for all X, which would reveal a smaller role for the electronegativity in the H–I bond formation, we have to take into account the mean squared deviation (denoted in Fig. 5). We found some outstanding situations in the NH_4PbI_3 case, the calculations without and with empirical vdW corrections generate $\langle d_{H-I} \rangle = 2.9$–3.0 Å (in fact, smaller values are obtained for D3BJ, ≈ 2.88 Å), presenting exactly the expected behavior with the molecular centralization due to the higher N electronegativity, while the semi-empirical vdW corrections are more sensitive to the electrostatic interactions between the organic and inorganic parts, which distort the tetrahedral geometry with the molecular displacement from the
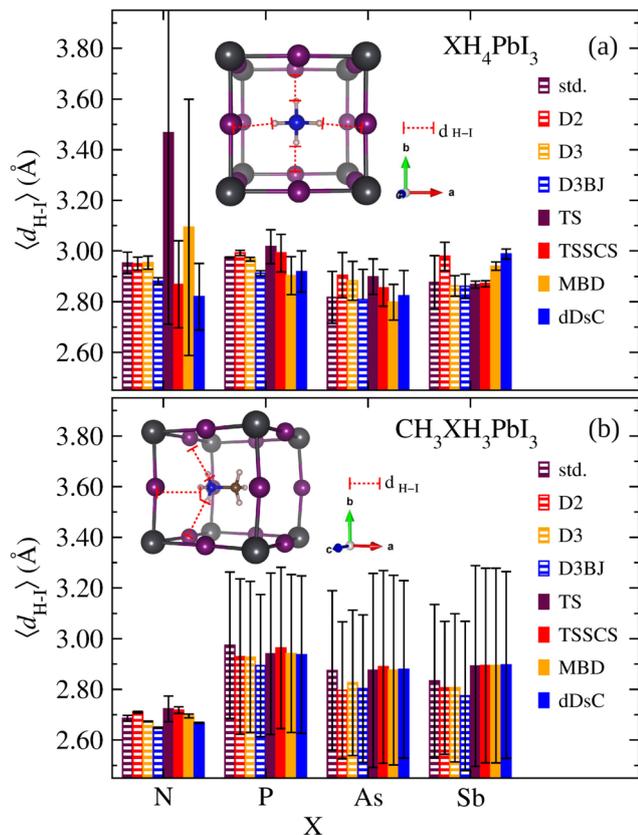
Fig. 5 The average H–I bond lengths, $\langle d_{H-I} \rangle$, considering the H atoms bonded to the X atoms, for (a) XH_4PbI_3 and (b) $CH_3XH_3PbI_3$ as a function of X (X = N, P, As, and Sb) for calculations without vdW (std) and with empirical (D2, D3, and D3BJ) or semi-empirical (TS, TSSCS, MBD, and dDsC) vdW corrections. The bars corresponding to the mean squared deviation are indicated for each system and its respective calculation method.

cavity center to the proximity of the cuboctahedral wall (approaching two H atoms). This trend is greatly exacerbated for NH_4PbI_3 in the case of TS description. Still, it is repeated, more attenuated for other semi-empirical vdW corrections, with at least one displaced H atom. Similar to NH_4PbI_3, for PH_4PbI_3, we observed higher $\langle d_{H-I} \rangle$ values and better behavior. However, for AsH_4PbI_3 and SbH_4PbI_3, all approximations are unanimous in describing the molecule as slightly displaced bilaterally with half of the H atoms being further away from the cuboctahedral wall and the remaining closer.

For the $CH_3XH_3PbI_3$ case, we observed a situation with an increased influence of the X electronegativity since we are dealing with a non-symmetrical and polar organic cation. Unlike the highest values presented for the smallest H–I distances for XH_4PbI_3, in the case of $CH_3XH_3PbI_3$ set, we observe that the minimum H–I bond values (considering the mean squared deviation) are around 2.57–2.69 Å, which characterizes hydrogen bonds, with the exception that the bonds are barely stretched for the case of high electronegativity of the N atom, which keeps the bonded H atoms gripped. In contrast, the X substitution by species with smaller electronegativities

has more pronounced H–I bonds. This result is in good agreement with the experimental neutron diffraction[97] and with the theoretical distance criterion of H···I < 3.0 Å to identify hydrogen bonding interactions of $CH_3NH_3PbI_3$.[100] Thus, with the $CH_3NH_3PbI_3$ exception, the other systems present the three H atoms (from the N side) arranged with two of them closer to the cavity wall, while the third H atom is further away. The center of $CH_3XH_3^+$ deviates from the cavity center so that the X end is closer to the vertex, consequently the three H from the $CH_3XH_3^+$ group are closer to the three halide anions, which significantly favor the development of H(N)···I bonds.

3.5 Energy gaps

To fully elucidate our MHP archetypes and the role played by vdW corrections, in addition to aspects of thermodynamic stability and structural changes, it is necessary to access the electronic structure of these systems *via* energy gap, E_g, calculations. For this purpose, we have taken into account three calculation sets for the XH_4PbI_3 and $CH_3XH_3PbI_3$ paragon structures resulting from the structural optimization without vdW correction and including the different empirical and semi-empirical vdW corrections, *i.e.*, calculations based solely on the DFT, including SOC (DFT + SOC), and with the relativistic quasiparticle correction (DFT-1/2) combined with SOC (DFT-1/2+SOC), as shown in Table 1. The vdW corrections indirectly obtain the gap energies since their role is predominant in the structural description, especially of the inorganic part. Consequently, it is necessary to analyze the possibility of band gap tuning *via* modification of the X species in MHPs; for the same X, the different structural motifs coming from the different vdW corrections must be considered as well.

From our energy gap results, we find that the standard DFT-based methods (here, using PBE), despite the unphysical self-coulombic repulsion,[101] lead to a reasonable description of the MHP band gaps, however, as an artificial effect from cancellation of errors, which can occur for materials formed by Pb^{2+} cations.[102] When SOC is included, the gap energy is strongly underestimated, in agreement with literature results for $CH_3NH_3PbI_3$ systems.[27,84] With excellent cost-benefit, outstanding band gap results are obtained for MHPs when the DFT-1/2 approach is combined with SOC.[16,87] Specifically, in the case of $CH_3NH_3PbI_3$ perovskite, for which we can compare our DFT-1/2 + SOC results with the experimental results (E_g = 1.48–1.68 eV),[103–107] we have excellent agreement with the magnitude of deviations between 1.30 and 14.67%. Thus, from now on, we will focus our discussion on the band gap results obtained *via* DFT-1/2 + SOC.

In general, we observed a direct relationship between the local structural distortions and band gaps in the XH_4PbI_3 and $CH_3XH_3PbI_3$ systems, in which the organic cations indirectly contribute to the band gap, since they do not electronically influence the frontier orbitals. However, their nature (ionic size and electronegativity differences) has an additive role in reducing the symmetry of the inorganic framework. Consequently, the more distorted the structural motifs are, as evidenced by the larger differences between the smallest and

Table 1 Energy gaps (E_g) for XH_4PbI_3 and $CH_3XH_3PbI_3$ (X = N, P, As, and Sb) perovskites based on structures optimized within empirical (D2, D3, and D3BJ), semi-empirical (TS, TSSCS, MBD, and dDsC), and without (std) vdW corrections through DFT, DFT + SOC, and DFT-1/2 + SOC calculations

System		E_g (eV)							
		Std	**D2**	**D3**	**D3BJ**	**TS**	**TSSCS**	**MBD**	**dDsC**
NH_4PbI_3	DFT	1.87	1.69	1.69	1.81	1.38	1.43	1.43	1.43
	DFT + SOC	0.85	0.80	0.80	0.84	0.41	0.38	0.41	0.41
	DFT-1/2 + SOC	2.00	1.80	1.81	1.93	1.17	1.44	1.42	1.41
PH_4PbI_3	DFT	1.42	1.15	1.22	1.22	1.26	1.36	1.34	1.32
	DFT + SOC	0.31	0.41	0.13	0.12	0.14	0.26	0.25	0.23
	DFT-1/2 + SOC	1.41	1.09	1.19	1.17	1.22	1.35	1.32	1.30
AsH_4PbI_3	DFT	1.51	1.17	1.25	1.26	1.27	1.38	1.37	1.34
	DFT + SOC	0.45	0.13	0.15	0.19	0.16	0.30	0.30	0.27
	DFT-1/2 + SOC	1.54	1.12	1.22	1.24	1.24	1.39	1.37	1.32
SbH_4PbI_3	DFT	1.44	1.32	1.31	1.26	1.31	1.36	1.34	1.39
	DFT + SOC	0.32	0.30	0.21	0.18	0.22	0.26	0.28	0.34
	DFT-1/2 + SOC	1.44	1.28	1.28	1.23	1.29	1.36	1.33	1.38
		Std	**D2**	**D3**	**D3BJ**	**TS**	**TSSCS**	**MBD**	**dDsC**
$CH_3NH_3PbI_3$	DFT	1.63	1.66	1.51	1.47	1.46	1.50	1.51	1.55
	DFT + SOC	0.62	0.80	0.50	0.48	0.43	0.46	0.55	0.54
	DFT-1/2 + SOC	1.50	1.57	1.33	1.28	1.36	1.42	1.47	1.37
$CH_3PH_3PbI_3$	DFT	1.55	1.32	1.39	1.37	1.44	1.51	1.44	1.43
	DFT + SOC	0.40	0.21	0.28	0.24	0.31	0.36	0.31	0.29
	DFT-1/2 + SOC	1.53	1.29	1.38	1.33	1.42	1.43	1.43	1.48
$CH_3AsH_3PbI_3$	DFT	1.59	1.37	1.45	1.41	1.47	1.53	1.48	1.47
	DFT + SOC	0.40	0.22	0.28	0.24	0.35	0.39	0.34	0.33
	DFT-1/2 + SOC	1.59	1.34	1.44	1.38	1.48	1.56	1.51	1.49
$CH_3SbH_3PbI_3$	DFT	1.63	1.55	1.52	1.47	1.57	1.67	1.59	1.62
	DFT + SOC	0.51	0.66	0.45	0.41	0.51	0.52	0.53	0.65
	DFT-1/2 + SOC	1.65	1.64	1.56	1.50	1.61	1.61	1.61	1.68

largest Pb–I bonds and Pb–I–Pb angles in both equatorial and apical directions (Tables S4 and S5†), the larger the energy gaps. This fact is further evidenced by the band gap values obtained from the optimized structures using different vdW corrections. Additionally, as long-range empirical and semi-empirical corrections contribute towards highlighting the organic–inorganic interactions, there is an improvement in the description of distortions, which reflects a band gap reduction concerning the std calculations. This gap energy closing by vdW description agrees with the slight contraction of the lattice parameters (and volume reduction).

Thus, combining thermodynamic stability with the structural modifications resulting from different organic cations, we found some structures that are promising candidates, in particular, PH_4PbI_3, AsH_4PbI_3, and SbH_4PbI_3, all with band gaps ranging between 1.09 and 1.33 eV, which fall in the middle of the range for optimum photovoltaic efficiency. Besides the low gap, our archetype perovskites with large cations have the advantage that the cavity filling should oppose the water incorporation since it can avoid the degradation of perovskite solar cells.[18] However, it is worth mentioning the correlation between the increasing size of X in the CH_3XH_3 cation and a slight opening of band gaps by going from X = N to Sb, which is due to the employment of local distortions on the inorganic sublattice through the use of large organic cations.

4 Conclusion

The SimStack workflows are a testament to efficiency in computational materials science. By automating the intricate sequence of tasks—from cation selection and molecular geometry processing to electronic structure calculation and data compilation—SimStack significantly accelerates raw data production. More notably, the automated data transfer from the 'DB-Generator' to GitHub, followed by analysis in a Colab notebook, exemplifies a streamlined, end-to-end process that reduces the time to insight. This seamless integration of simulation, data management, and analysis within the SimStack framework promises to save researchers an enormous amount of time, thereby relieving them of the burden of tedious tasks and expediting innovation and discovery in materials science. By using the above workflows, we assessed the performance of the empirical and semi-empirical vdW corrections in designing organic cations of the XH_4PbI_3 and $CH_3XH_3PbI_3$ prototype perovskites *via* change of the X species (N, P, As, and Sb). In addition to the relativistic PBE-based calculations, we included the D2, D3, D3BJ, TS, TSSCS, MBD, and dDsC vdW approaches to describe the thermodynamic stability, structural properties of the organic and inorganic parts, and energy gaps, the latter using SOC calculations combined with the DFT-1/2 quasiparticle approximation. Our results reveal that the dispersive energy term contributes to improving the energy

stabilization of the studied systems. The thermodynamic feasibility was confirmed for both sets through an exothermic formation route based on the molecular precursors in the gas phase combined with $PbI_2(s)$, where the formation enthalpy magnitude decreases with X, and the most thermodynamically favorable compounds are obtained for X = N.

The stability trend was related to the nature of organic cations in the design process, *i.e.*, the feasibility of building XH_4PbI_3 and $CH_3XH_3PbI_3$ through different ionic sizes and electronegativities. As the octahedron stability implies a limited volume of the cuboctahedral cavities to accommodate the organic cations, we estimated the ionic radii for symmetrical (XH_4^+) and nonspherically symmetric $(CH_3XH_3^+)$ cations, which follow the atomic size increase of pnictogens. Our archetypal models have a Goldschmidt criterion that points to a ionic size mismatch in the XH_4PbI_3 $(CH_3XH_3PbI_3)$ group, where NH_4PbI_3 $(CH_3NH_3PbI_3)$ lies outside (inside) the stable region for perovskites. With the expectation that small organic cations fit better into the structure (except NH_4PbI_3), consequently, in addition to $CH_3NH_3PbI_3$, some hypothetical perovskites with phosphonium, arsonium, and stibonium are predicted.

We identified a situation of cation confinement in the inorganic cavity, with slight structural changes due to different vdW flavors concerning the standard calculations (without vdW), *e.g.*, it was ≤0.37% for the tolerance factor. However, only including the X electronegativity, it was possible to understand the thermodynamic stability trend, *i.e.*, from N up to Sb, the ionic radius increases and the electronegativity decreases in the organic cation composition, which lead to a decrease in thermodynamic stability (also evidenced by the tolerance factor), since there is an intensification of the ionic electrostatic interaction with the inorganic framework, resulting in larger structural distortions. Therefore, it was possible to verify a slight (average) increase in the structural volume (lattice parameters) with the X atomic number that results from the cavity deformation to accommodate the organic cations.

The empirical vdW corrections (especially D2) showed a more significant contraction of lattice parameters than semiempirical vdW and standard calculations. Consequently, the vdW corrections indirectly affect the structural stability by improving the treatment of organic–inorganic interactions since the structural motifs showed octahedral distortions and hydrogen bond formation. Despite having the same inorganic framework for all archetypes, the local distortions of the octahedra were evidenced by deformations in equatorial and apical Pb–I bonds and Pb–I–Pb angles concerning the expected well-behaved Platonic case. In connection to that, we have the bridging bond between the electron-donating element in the organic cation (X) and H atoms, forming a bridge with the I, causing the (bilateral) molecular displacement from the cavity center. The organic cations indirectly contribute to the band gap since they induce the local structural distortions, directly affecting the XH_4PbI_3 and $CH_3XH_3PbI_3$ band gaps. The more distorted structural motifs showed more significant energy gaps, considering all optimized structures through different vdW approaches. Thus, considering the complete picture, the vdW correction allowed an improved description of hybrid

MHPs with some up-and-coming new hypothetical candidates, *e.g.*, PH_4PbI_3, AsH_4PbI_3, and SbH_4PbI_3.

Data availability

The authors confirm that the data supporting this study's findings are available in the article and the ESI† and upon request. The Halide-Perovskite Workflow is also available to the public *via* the Halide-Perovskite repository at **https://github.com/KIT-Workflows/Halide-Perovskites**.

Author contributions

C. R. C. R. analyzed the data, wrote the first version of the manuscript, and developed the workflows to automate the calculations. W. W. helped develop ideas and provided computational/software resources. M. J. P. wrote the first version of the manuscript and helped develop ideas and data analyses. A. C. D. helped develop ideas and helped with data analysis. C. M. O. B. helped develop ideas and helped with data analysis. L. O. A. helped develop ideas and helped with data analysis. D. G. S. carried out the DFT calculations, analyzed the data, made the graphs, and wrote the first version of the manuscript. All authors performed subsequent revisions of the manuscript.

Conflicts of interest

There are no conflicts to declare.

Acknowledgements

Notes and references

1 A. Kojima, K. Teshima, Y. Shirai and T. Miyasaka, *J. Am. Chem. Soc.*, 2009, **131**, 6050–6051.

2 H.-S. Kim, C.-R. Lee, J.-H. Im, K.-B. Lee, T. Moehl, A. Marchioro, S.-J. Moon, R. Humphry-Baker, J.-H. Yum, J. E. Moser, M. Gratzel and N.-G. Park, *Sci. Rep.*, 2012, **2**, 591.

3 M. Grätzel, *Nature*, 2014, **13**, 838–842.

4 Z. Chen, B. Turedi, A. Y. Alsalloum, C. Yang, X. Zheng, I. Gereige, A. AlSaggaf, O. F. Mohammed and O. M. Bakr, *ACS Energy Lett.*, 2019, **4**, 1258–1259.

5 X. Li, J. Du, H. Duan, H. Wang, L. Fan, Y. Sun, Y. Sui, J. Yang, F. Wang and L. Yang, *Nano Res.*, 2022, **15**, 1375–1382.

6 J. Park, J. Kim, H.-S. Yun, M. J. Paik, E. Noh, H. J. Mun, M. G. Kim, T. J. Shin and S. I. Seok, *Nature*, 2023, **616**, 724–730.

7 D. B. Mitzi, *J. Chem. Soc., Dalton Trans.*, 2001, 1–12.

8 J. S. Manser, J. A. Christians and P. V. Kamat, *Chem. Rev.*, 2016, **116**, 12956–13008.

9 B. Saparov and D. B. Mitzi, *Chem. Rev.*, 2016, **116**, 4558–4596.

10 R. Gottesman, L. Gouda, B. S. Kalanoor, E. Haltzi, S. Tirosh, E. Rosh-Hodesh, Y. Tischler, A. Zaban, C. Quarti, E. Mosconi and F. De Angelis, *J. Phys. Chem. Lett.*, 2015, **6**, 2332–2338.

11 A. Kovalsky, L. Wang, G. T. Marek, C. Burda and J. S. Dyck, *J. Phys. Chem. C*, 2017, **121**, 3228–3233.

12 F. Hao, C. C. Stoumpos, R. P. H. Chang and M. G. Kanatzidis, *J. Am. Chem. Soc.*, 2014, **136**, 8094–8099.

13 F. Zheng, L. Z. Tan, S. Liu and A. M. Rappe, *Nano Lett.*, 2016, **16**, 7316.

14 T. Etienne, E. Mosconi and F. De Angelis, *J. Phys. Chem. Lett.*, 2016, **7**, 1638–1645.

15 T. Krishnamoorthy, H. Ding, C. Yan, W. L. Leong, T. Baikie, Z. Zhang, M. Sherburne, S. Li, M. Asta, N. Mathews and S. G. Mhaisalkar, *J. Mater. Chem. A*, 2015, **3**, 23829–23832.

16 L. O. de Araujo, F. P. Sabino, C. R. C. Rêgo and D. Guedes-Sobrinho, *J. Phys. Chem. Lett.*, 2021, **12**, 7245–7251.

17 I. Borriello, G. Cantele and D. Ninno, *Phys. Rev. B:Condens. Matter Mater. Phys.*, 2008, **77**, 235214.

18 J. H. Noh, S. H. Im, J. H. Heo, T. N. Mandal and S. I. Seok, *Nano Lett.*, 2013, **13**, 1764–1769.

19 D. Guedes-Sobrinho, I. Guilhon, M. Marques and L. K. Teles, *Sci. Rep.*, 2019, **9**, 11061.

20 L. O. de Araujo, C. R. Rêgo, W. Wenzel, C. M. de Oliveira Bastos, M. J. Piotrowski, A. C. Dias and D. Guedes-Sobrinho, *J. Alloys Compd.*, 2024, **992**, 174485.

21 M. R. Filip, G. E. Eperon, H. J. Snaith and F. Giustino, *Nat. Commun.*, 2014, **5**, 5757.

22 M. R. Filip, C. Verdi and F. Giustino, *J. Phys. Chem. C*, 2015, **119**, 25209–25219.

23 J. M. Frost, K. T. Butler, F. Brivio, C. H. Hendon, M. v. Schilfgaarde and A. Walsh, *Nano Lett.*, 2014, **14**, 2584–2590.

24 A. Amat, E. Mosconi, E. Ronca, C. Quarti, P. Umari, M. K. Nazeeruddin, M. GrÃtzel and F. De Angelis, *Nano Lett.*, 2014, **14**, 3608–3616.

25 F. E.-M. E. T. Bentria, S. N. Rashkeev, S. Kais and F. H. Alharbi, *Sci. Rep.*, 2016, **6**, 30305.

26 F. Brivio, K. T. Butler, A. Walsh and M. van Schilfgaarde, *Phys. Rev. B:Condens. Matter Mater. Phys.*, 2014, **89**, 155204.

27 P. Umari, E. Mosconi and F. De Angelis, *Sci. Rep.*, 2014, **4**, 4467.

28 C. Motta, F. El-Mellouhi, S. Kais, N. Tabet, F. Alharbi and S. Sanvito, *Nat. Commun.*, 2015, **6**, 7026.

29 F. E.-M. E. T. Bentria, A. Marzouk, S. N. Rashkeev, S. Kais and F. H. Alharbi, *npj Comput. Mater.*, 2016, **2**, 16035.

30 D. A. Egger and L. Kronik, *J. Phys. Chem. Lett.*, 2014, **5**, 2728–2733.

31 K. Lejaeghere, V. V. Speybroeck, G. V. Oost and S. Cottenier, *Crit. Rev. Solid State Mater. Sci.*, 2014, **39**, 1–24.

32 K. Lejaeghere, G. Bihlmayer, T. Björkman, P. Blaha, S. Blügel, V. Blum, D. Caliste, I. E. Castelli, S. J. Clark, A. D. Corso, S. de Gironcoli, T. Deutsch, J. K. Dewhurst, I. D. Marco, C. Draxl, M. Dulak, O. Eriksson, J. A. Flores-Livas, K. F. Garrity, L. Genovese, P. Giannozzi, M. Giantomassi, S. Goedecker, X. Gonze, O. Granäs, E. K. U. Gross, A. Gulans, F. Gygi, D. R. Hamann, P. J. Hasnip, N. A. W. Holzwarth, D. Iusan, D. B. Jochym, F. Jollet, D. Jones, G. Kresse, K. Koepernik, E. Kücükbenli, Y. O. Kvashnin, I. L. M. Locht, S. Lubeck, M. Marsman, N. Marzari, U. Nitzsche, L. Nordström, T. Ozaki, L. Paulatto, C. J. Pickard, W. Poelmans, M. I. J. Probert, K. Refson, M. Richter, G.-M. Rignanese, S. Saha, M. Scheffler, M. Schlipf, K. Schwarz, S. Sharma, F. Tavazza, P. Thunström, A. Tkatchenko, M. Torrent, D. Vanderbilt, M. J. van Setten, V. V. Speybroeck, J. M. Wills, J. R. Yates, G.-X. Zhang and S. Cottenier, *Science*, 2016, **351**, 1415.

33 C. R. C. Rêgo, L. N. Oliveira, P. Tereshchuk and J. L. F. Da Silva, *J. Phys.: Condens. Matter*, 2015, **27**, 415502.

34 C. R. C. Rêgo, L. N. Oliveira, P. Tereshchuk and J. L. F. Da Silva, *J. Phys.: Condens. Matter*, 2016, **28**, 129501.

35 A. Tkatchenko and M. Scheffler, *Phys. Rev. Lett.*, 2009, **102**, 073005.

36 A. Tkatchenko, R. A. DiStasio, R. Car and M. Scheffler, *Phys. Rev. Lett.*, 2012, **108**, 236402.

37 A. Tkatchenko, A. Ambrosetti and R. A. DiStasio, *J. Chem. Phys.*, 2013, **138**, 074106.

38 S. Grimme, A. Hansen, J. G. Brandenburg and C. Bannwarth, *Chem. Rev.*, 2016, **116**, 5105–5154.

39 M. Dion, H. Rydberg, E. Schröder, D. C. Langreth and B. I. Lundqvist, *Phys. Rev. Lett.*, 2004, **92**, 109902.

40 G. Román-Pérez and J. M. Soler, *Phys. Rev. Lett.*, 2009, **103**, 096102.

41 J. Klimeš, D. R. Bowler and A. Michaelides, *Phys. Rev. B:Condens. Matter Mater. Phys.*, 2011, **83**, 195131.

42 S. Grimme, *J. Comput. Chem.*, 2006, **27**, 1787–1799.

43 S. Grimme, J. Antony, S. Ehrlich and H. Krieg, *J. Chem. Phys.*, 2010, **132**, 154104.

44 S. N. Steinmann and C. Corminboeuf, *J. Chem. Phys.*, 2011, **134**, 044117.

45 S. N. Steinmann and C. Corminboeuf, *J. Chem. Theory Comput.*, 2011, **7**, 3567–3577.

46 J. Klimeš and A. Michaelides, *J. Chem. Phys.*, 2012, **137**, 120901.

47 K. Berland, V. R. Cooper, K. Lee, E. Schröder, T. Thonhauser, P. Hyldgaard and B. I. Lundqvist, *Rep. Prog. Phys.*, 2015, **78**, 066501.

48 J. Park, B. D. Yu and S. Hong, *Curr. Appl. Phys.*, 2015, **15**, 885–891.

49 S. Grimme, S. Ehrlich and L. Goerigk, *J. Comput. Chem.*, 2011, **32**, 1456–1465.

50 W. Reckien, F. Janetzko, M. F. Peintinger and T. Bredow, *J. Comput. Chem.*, 2012, **33**, 2023–2031.

51 A. Ambrosetti, A. M. Reilly, R. A. DiStasio and A. Tkatchenko, *J. Chem. Phys.*, 2014, **140**, 18A508.

52 F. L. Hirshfeld, *Theor. Chim. Acta*, 1977, **44**, 129–138.

53 L. G. Ferreira, M. Marques and L. K. Teles, *Phys. Rev. B:Condens. Matter Mater. Phys.*, 2008, **78**, 125116.

54 T. Baikie, Y. Fang, J. M. Kadro, M. Schreyer, F. Wei, S. G. Mhaisalkar, M. Graetzel and T. J. White, *J. Mater. Chem. A*, 2013, **1**, 5628–5641.

55 F. Brivio, A. B. Walker and A. Walsh, *APL Mater.*, 2013, **1**, 042111.

56 Y. Zong, Y. Zhou, M. Ju, H. F. Garces, A. R. Krause, F. Ji, G. Cui, X. C. Zeng, N. P. Padture and S. Pang, *Angew. Chem., Int. Ed.*, 2016, **55**, 14723–14727.

57 W. Huang, J. S. Manser, S. Sadhu, P. V. Kamat and S. Ptasinska, *J. Phys. Chem. Lett.*, 2016, **7**, 5068–5073.

58 C. R. C. Rêgo, J. Schaarschmidt, T. Schlöder, M. Penaloza-Amion, S. Bag, T. Neumann, T. Strunk and W. Wenzel, *Front. Mater.*, 2022, **9**, 877597.

59 S. P. Huber, S. Zoupanos, M. Uhrin, L. Talirz, L. Kahle, R. Häuselmann, D. Gresch, T. Müller, A. V. Yakutovich, C. W. Andersen, F. F. Ramirez, C. S. Adorf, F. Gargiulo, S. Kumbhar, E. Passaro, C. Johnston, A. Merkys, A. Cepellotti, N. Mounet, N. Marzari, B. Kozinsky and G. Pizzi, *Sci. Data*, 2020, **7**, 300.

60 J. Janssen, S. Surendralal, Y. Lysogorskiy, M. Todorova, T. Hickel, R. Drautz and J. Neugebauer, *Comput. Mater. Sci.*, 2019, **163**, 24–36.

61 J. Schaarschmidt, J. Yuan, T. Strunk, I. Kondov, S. P. Huber, G. Pizzi, L. Kahle, F. T. Bölle, I. E. Castelli, T. Vegge, F. Hanke, T. Hickel, J. Neugebauer, C. R. C. Rêgo and W. Wenzel, *Adv. Energy Mater.*, 2021, **12**, 2102638.

62 S. Bekemeier, C. R. Caldeira Rêgo, H. L. Mai, U. Saikia, O. Waseda, M. Apel, F. Arendt, A. Aschemann, B. Bayerlein, R. Courant, G. Dziwis, F. Fuchs, U. Giese, K. Junghanns, M. Kamal, L. Koschmieder, S. Leineweber, M. Luger, M. Lukas, J. Maas, J. Mertens, B. Mieller, L. Overmeyer, N. Pirch, J. Reimann, S. Schröck, P. Schulze, J. Schuster, A. Seidel, O. Shchyglo, M. Sierka, F. Silze, S. Stier, M. Tegeler, J. F. Unger, M. Weber, T. Hickel and J. Schaarschmidt, *Adv. Eng. Mater.*, 2025, 2402149.

63 G. R. Da Silva, J. P. Cerqueira Felix, C. R. C. Rêgo, A. C. Dias, C. M. de O. Bastos, M. J. Piotrowski and D. Guedes-Sobrinho, *Sci. Rep.*, 2025, **15**, 1939.

64 H. Pecinatto, C. R. C. Rêgo, W. Wenzel, C. A. Frota, B. M. S. Perrone, M. J. Piotrowski, D. Guedes-Sobrinho, A. C. Dias, C. Mota, M. S. S. Gusmão and H. O. Frota, *Sci. Rep.*, 2023, **13**, 17157.

65 M. Soleymanibrojeni, C. R. Caldeira Rego, M. Esmaeilpour and W. Wenzel, *J. Mater. Chem. A*, 2024, **12**, 2249–2266.

66 B. Mieller, M. Valavi and C. R. Caldeira Rêgo, *Adv. Eng. Mater.*, 2024, 2400872.

67 L. O. de Araujo, C. R. C. Rêgo, W. Wenzel, M. J. Piotrowski, A. C. Dias and D. Guedes-Sobrinho, *npj Comput. Mater.*, 2024, **10**, 146.

68 J. F. Dalmedico, D. N. Silveira, L. O. de Araujo, W. Wenzel, C. R. C. Rêgo, A. C. Dias, D. Guedes-Sobrinho and M. J. Piotrowski, *ChemPhysChem*, 2024, **25**, e202400118.

69 M. Mostaghimi, C. R. C. Rêgo, R. Haldar, C. Wöll, W. Wenzel and M. Kozlowska, *Front. Mater.*, 2022, **9**, 840644.

70 P. Hohenberg and W. Kohn, *Phys. Rev.*, 1964, **136**, B864–B871.

71 W. Kohn and L. J. Sham, *Phys. Rev.*, 1965, **140**, A1133–A1138.

72 J. P. Perdew, J. A. Chevary, S. H. Vosko, K. A. Jackson, M. R. Pederson, D. J. Singh and C. Fiolhais, *Phys. Rev. B:Condens. Matter Mater. Phys.*, 1992, **46**, 6671–6687.

73 J. P. Perdew, K. Burke and M. Ernzerhof, *Phys. Rev. Lett.*, 1996, **77**, 3865–3868.

74 G. Kresse and J. Hafner, *Phys. Rev. B:Condens. Matter Mater. Phys.*, 1993, **48**, 13115–13118.

75 G. Kresse and J. Furthmüller, *Phys. Rev. B:Condens. Matter Mater. Phys.*, 1996, **54**, 11169–11186.

76 T. Bučko, S. Lèbegue, J. Hafner and J. G. Ángyán, *Phys. Rev. B:Condens. Matter Mater. Phys.*, 2013, **87**, 064110.

77 T. Bučko, S. Lèbegue, J. Hafner and J. G. Ángyán, *J. Chem. Theory Comput.*, 2013, **9**, 4293–4299.

78 P. E. Blöchl, *Phys. Rev. B:Condens. Matter Mater. Phys.*, 1994, **50**, 17953–17979.

79 G. Kresse and D. Joubert, *Phys. Rev. B:Condens. Matter Mater. Phys.*, 1999, **59**, 1758–1775.

80 J. Hafner, *J. Comput. Chem.*, 2008, **29**, 2044–2078.

81 D. D. Koelling and B. N. Harmon, *J. Phys. C: Solid State Phys.*, 1977, **10**, 3107–3114.

82 T. Takeda, *Z. Phys. B*, 1978, **32**, 43–48.

83 J. Even, L. Pedesseau, M. Dupertuis, J. Jancu and C. Katan, *Phys. Rev. B:Condens. Matter Mater. Phys.*, 2012, **86**, 205301.

84 J. Even, L. Pedesseau, J.-M. Jancu and C. Katan, *J. Phys. Chem. Lett.*, 2013, **4**, 2999–3005.

85 J. Even, L. Pedesseau, C. Katan, M. Kepenekian, J. Lauret, D. Sapori and E. Deleporte, *J. Phys. Chem. C*, 2015, **119**, 10161–10177.

86 D. Guedes-Sobrinho, I. Guilhon, M. Marques and L. K. Teles, *J. Phys. Chem. Lett.*, 2019, **10**, 4245–4251.

87 L. Octavio de Araujo, C. R. C. Rêgo, W. Wenzel, F. P. Sabino and D. Guedes-Sobrinho, *J. Phys. Chem. C*, 2022, **126**, 2131–2140.

88 R. E. Wasylishen, O. Knop and J. B. Macdonald, *Solid State Commun.*, 1985, **56**, 581–582.

89 S. R. Raga, L. K. Ono and Y. Qi, *J. Mater. Chem. A*, 2016, **4**, 2494–2500.

90 L. Pauling, *The Nature of the Chemical Bond*, Cornell University Press, Ithaca, 1960.

91 R. D. Shannon, *Acta Crystallogr., Sect. A: Found. Crystallogr.*, 1976, **32**, 751–767.

92 G. Kieslich, S. Sun and A. K. Cheetham, *Chem. Sci.*, 2014, **5**, 4712–4715.

93 V. M. Goldschmidt, *Naturwissenschaften*, 1926, **14**, 477–485.

94 G. Kieslich, S. Sun and A. K. Cheetham, *Chem. Sci.*, 2015, **6**, 3430–3433.

95 W. M. Haynes, *CRC Handbook of Chemistry and Physics*, Taylor & Francis Group, 95th edn, 2014.

96 T. A. Manz and N. G. Limas, *RSC Adv.*, 2016, **6**, 47771–47801.

97 M. T. Weller, O. J. Weber, P. F. Henry, A. M. Di Pumpo and T. C. Hansen, *Chem. Commun.*, 2015, **51**, 4180–4183.

98 C. C. Stoumpos, C. D. Malliakas and M. G. Kanatzidis, *Inorg. Chem.*, 2013, **52**, 9019–9038.

99 J.-H. Lee, N. C. Bristowe, J. H. Lee, S.-H. Lee, P. D. Bristowe, A. K. Cheetham and H. M. Jang, *Chem. Mater.*, 2016, **28**, 4259–4266.

100 J.-H. Lee, N. C. Bristowe, P. D. Bristowe and A. K. Cheetham, *Chem. Commun.*, 2015, **51**, 6434–6437.

101 J. P. Perdew and A. Zunger, *Phys. Rev. B:Condens. Matter Mater. Phys.*, 1981, **23**, 5048–5079.

102 S.-H. Wei and A. Zunger, *Phys. Rev. B:Condens. Matter Mater. Phys.*, 1997, **55**, 13605.

103 S. Singh, C. Li, F. Panzer, K. L. Narasimhan, A. Graeser, T. P. Gujar, A. Köhler, M. Thelakkat, S. Huettner and D. Kabra, *J. Phys. Chem. Lett.*, 2016, **7**, 3014–3021.

104 A. M. A. Leguy, P. Azarhoosh, M. I. Alonso, M. Campoy-Quiles, O. J. Weber, J. Yao, D. Bryant, M. T. Weller, J. Nelson, A. Walsh, M. van Schilfgaarde, *et al.*, *Nanoscale*, 2016, **8**, 6317–6327.

105 L. Q. Phuong, Y. Yamada, M. Nagai, N. Maruyama, A. Wakamiya and Y. Kanemitsu, *J. Phys. Chem. Lett.*, 2016, **7**, 2316–2321.

106 L. Jiang, T. Wu, L. Sun, Y.-J. Li, A. Li, R. Lu, K. Zou and W.-Q. Deng, *J. Phys. Chem. C*, 2017, **121**, 24359–24364.

107 F. Palazon, D. Pérez-del Rey, B. DÃnekamp, C. Dreessen, M. Sessolo, P. P. Boix and H. J. Bolink, *Adv. Mater.*, 2019, **31**, 1902692.